LA-UR-19-26679 (Accepted Manuscript)

Modeling the Magnetopause Shadowing Loss During the June 2015 Dropout Event

Tu, Weichao
Xiang, Zheng
Morley, Steven Karl

To be published in: Geophysical Research Letters

DOI to publisher's version: 10.1029/2019GL084419

Permalink to record: http://permalink.lanl.gov/object/view?what=info:lanl-repo/lareport/LA-UR-19-26679

Tu Weichao (Orcid ID: 0000-0003-4547-3269)
Morley Steven, K. (Orcid ID: 0000-0001-8520-0199)

Modeling the Magnetopause Shadowing Loss during the June 2015 Dropout Event

Weichao Tu[1], Zheng Xiang[1,2], and S. K. Morley[3]

[1] Department of Physics and Astronomy, West Virginia University, Morgantown, West Virginia, USA

[2] Laboratory for Atmospheric and Space Physics, University of Colorado Boulder, Boulder, Colorado, USA

[3] Space Science and Applications, Los Alamos National Laboratory, Los Alamos, New Mexico, USA

Key Points:

- A radial diffusion model with event-specific and K-dependent LCDS and recent D_{LL} is used to simulate the electron magnetopause shadowing loss.

This is the author manuscript accepted for publication and has undergone full peer review but has not been through the copyediting, typesetting, pagination and proofreading process, which may lead to differences between this version and the Version of Record. Please cite this article as doi: 10.1029/2019GL084419

- The model captures the fast shadowing loss of electrons at high L* and the initial adiabatic loss of the high-energy storage ring at low L*.
- Future inclusion of the EMIC wave scattering process is needed to model the observed further depletion of the storage ring.

Abstract

Fast dropout of relativistic and ultrarelativistic electrons at both high and low L* regions were observed during the intense coronal mass ejection driven storm in June 2015. An improved radial diffusion model, using an event-specific Last Closed Drift Shell (LCDS) and newly-available radial diffusion coefficients (D_{LL}), is implemented to simulate the magnetopause shadowing loss of electrons. The model captures the fast shadowing loss of electrons well at high L* regions after both interplanetary shocks, and reproduces the initial adiabatic loss of the high-energy storage ring at low L* regions after the second strong shock. We show for the first time that using the event-specific and K-dependent LCDS and improved D_{LL} is critical to reproduce the observed dropout features, including the timing, location, and the butterfly electron pitch angle distribution. Future inclusion of the EMIC wave scattering process is needed to model the observed further depletion of the storage ring.

1. Introduction

Earth's radiation belts, which contain energetic electrons and protons that are trapped by the geomagnetic field, present a hazardous radiative environment for spacecrafts operating within [e.g., Baker, 2000; Lanzerotti, 2001]. Since their discovery in 1958, understanding the governing processes, and simulating and eventually predicting the radiation belt dynamics have been the targets that space physicists have long pursued [see review papers: Millan and Baker, 2012; Shprits et al., 2008a, b; and references therein]. The NASA Van Allen Probes mission has enabled new and higher-fidelity description of the radiation belts. One type of the remarkable variations of Earth's outer radiation belt is called radiation belt dropout, during which the MeV electron fluxes are observed to drop by orders of magnitude on time scales of a few hours or less [e.g., Onsager et al., 2002; Tu et al., 2009, 2010, 2014; Morley et al., 2010a,b; Turner et al., 2012; Shprits et al, 2016; Xiang et al., 2017, 2018]. The fundamental question is where the electrons go during the dropouts. It is known that electrons can be lost by precipitation into the atmosphere due to interactions with various magnetospheric waves including plasmaspheric hiss, chorus, and electromagnetic ion cyclotron (EMIC) waves, with MeV electrons most effectively scattered by EMIC waves [e.g., Shprits et al, 2016; Xiang et al., 2017, 2018], or lost through the outer boundary of magnetosphere, the magnetopause [e.g., Turner et al., 2012; Olifer et al., 2018]. The latter mechanism is called magnetopause shadowing, usually due to solar wind compression of the magnetopause combined with outward radial diffusion of electrons caused by the sharp radial gradient in electron distributions [e.g., Loto'aniu et al., 2010; Turner et al., 2012]. Determining which of these two mechanisms is mainly responsible for the observed radiation belt electron dropout is one of the most important outstanding questions in radiation belt studies. However, to resolve this question requires quantitative physical modeling [e.g., Ozeke, et al., 2017; Xiang et al., 2017, 2018]. In this paper we select the June 22-23, 2015 dropout event for a detailed modeling study.

The June 2015 event is one of the most powerful Coronal Mass Ejection (CME) driven storms in the Van Allen Probes era, with Dst reaching -204 nT as shown in Panel (a4) of Figure 1. Panels (a1)-(a3) plot the energetic electron fluxes observed by the REPT (Relativistic Electron-Proton Telescope [Baker et al., 2013]) instrument on board of Van Allen Probes, at energies of 1.8, 4.2, and 6.3 MeV respectively. The fluxes in color are at 90^o local pitch angle and distributed vs. time (two days) and L (McIlwain L [McIlwain, 1961] calculated using the OP77Q external field model [Olson & Pfitzer, 1977] and IGRF internal field model [Finlay et al., 2010]). For this event, Van Allen Probe A is leading Probe B by about an hour (which means Probe A crosses a given L about an hour earlier than Probe B), providing an excellent opportunity to resolve the spatial and temporal evolutions of electron fluxes. Panels (b1) and (b2) show the interplanetary magnetic field (IMF) B_z and solar wind dynamic pressure (P_{dyn}) during the event, which illustrate two interplanetary shocks that struck the Earth during June 22, as marked by the two vertical red lines in Figure 1. The first shock arrived at ~05:30 UT, which leads to some decrease of the MeV electrons at large L regions as shown in the left flux panels. The second shock arrived at ~18:36UT, which is much more powerful with solar wind P_{dyn} reaching about 60 nPa and IMF B_z dropped to about -40 nT. As shown in the left flux panels, the second strong shock leads to a sudden and nearly complete depletion of outer zone electrons outside L~3.5 and across a wide range of energies. In addition, by looking closer at the lower L regions in the 4.2 MeV and 6.3 MeV flux plots we see a high-energy storage ring between L=2.5 and 3.5, which had been present since early June (not shown in the figure). Zooming in on the low L regions (shown in the red boxes in Panels (a3) and (a4)), we find the storage ring shows a two-step loss process: an initial drop right after the second shock as observed by Probe A (the leading probe), and then a complete depletion at about an hour later as observed by Probe B. The storage ring is present at 4.2-7.7 MeV as measured by REPT and the two-step loss shows up over that full range of energies.

The rapid and deep dropout of relativistic and ultrarelativistic electrons observed at both high and low L regions during this strong CME-driven storm has attracted a lot attention. Baker et al. [2016] first reported the fast and complete electron depletions over a wide range of L and energies observed during the event. They implied that magnetopause shadowing due to the strong CME shock could play an important role in the loss of radiation belt electrons at high L regions, even though there was little discussion of the loss mechanisms for the storage ring at low L regions. Xiang et al. [2017] performed a detailed analysis of the event based on the evolution of the electron Phase Space Density (PSD) vs. L* profiles (where L* is the Roederer L related to the third adiabatic invariant [Roederer, 1970] calculated using the TS04 storm time model [Tsyganenko and Sitnov, 2005]). They also suggested that magnetopause shadowing could be the dominant loss mechanism at high L* regions, but they found the combination of magnetopause shadowing and outward radial diffusion could not explain the PSD loss at low L* regions which requires additional loss mechanisms. Qin et al. [2019] focused on the depletion of high-energy storage ring during this event and argued that pitch angle scattering by H^+ band EMIC waves could explain the rapid loss of >4 MeV electrons at low L. However, none of the previous work conducted physical modeling of the electron dynamics during this dropout event to compare quantitatively with observations. In addition, the two-step losses of the storage ring were not studied in detail. Here for the first time we quantitatively model the magnetopause shadowing loss during the June 2015 dropout event with realistic inputs, to reproduce the observed loss features at different L regions as described above and to resolve the relative importance of different loss mechanisms.

2. Event Analysis

To prepare for physical modeling, we first use the LANLGeoMag library to calculate the Last Closed Drift Shell (LCDS) of energetic electrons which is an important indicator for magnetopause shadowing [see Albert et al., 2018]. Panel (b3) of Figure 1 illustrates the LCDS at different K (the second adiabatic invariant) values calculated using the TS04 model, with increasing K from blue to red. We see that LCDS is K-dependent, since L* is pitch angle-dependent due to drift shell splitting in realistic geomagnetic fields. The LCDS at all K values were pushed to inside L*=4 by the second strong shock (due to very high solar wind P_{dyn} and strong southward IMF B_z) and stayed low for a couple of hours. The low LCDS could account for the fast depletion of outer belt electrons after the second shock. In addition, the LCDS shows a strong K-dependence during most of the event, with larger LCDS at higher K (corresponding to lower equatorial pitch angles). This is consistent with the classic drift shell splitting picture of electrons starting from the same field line on the dayside, with lower equatorial pitch angle electrons splitting to a smaller drift shell or L* value in realistic non-axisymmetric magnetic fields [Roederer, 1970]. This strong K-dependence in LCDS is evident between the first and second shocks (the two vertical red lines), where the LCDS at low K values can drop to close to L*=4 but the LCDS at high K are outside L*=6. Consequently, the K-dependent magnetopause shadowing would lead to more electron loss at low K values than at high K, where a butterfly pitch angle distribution of electrons would be expected. Panel (b4) shows the 1.8 MeV electron fluxes versus time and local pitch angle observed by Van Allen Probe A along its orbit. We see that the fluxes show a moderate drop between subsequent apogees, marked by the black arrows, which is consistent with Panel (a1) between the two shocks. Additionally, the fluxes at the apogees illustrate clear butterfly pitch angle distributions, consistent with the effects from K-dependent magnetopause shadowing losses. The extremely low LCDS values during the event and the corresponding butterfly pitch angle distributions of electrons provide strong evidence that K-dependent magnetopause shadowing plays a critical role for the electron dropout during the June 2015 event.

In addition, the observed electron fluxes are converted to electron Phase Space Density (PSD) as a function of the three adiabatic invariants (μ, K, and L*) for physical modeling. REPT fluxes are combined with lower-energy (<1.8 MeV) fluxes from MagEIS instrument for PSD calculation and all the invariants are calculated using TS04 model fields. Panel (a1) of Figure 2 shows the calculated PSD at μ=1318 MeV/G and K=0.03 $G^{1/2}R_E$ (corresponding to approximately 2.1 MeV and 68° equatorial pitch angle electrons at L= 4 in a dipole), distributed versus time and L*. The two shock arrivals are marked as vertical red lines and the LCDS at K=0.03 $G^{1/2}R_E$ is overplotted as a black dashed curve. By comparing the PSD plot with the flux plots in Figure 1, we see large gaps in the PSD values. The PSD gaps at high L* are due to low LCDS after the second shock, since electrons are on open drift shells outside LCDS thus L* is undefined (note there are a small number of PSD values outside LCDS due to uncertainties in the L* calculation with TS04 model). In addition, the PSD gaps at low L* regions are due to limited coverage of the measured fluxes in equatorial pitch angles during certain parts of the orbits (Van Allen Probes are located off the magnetic equator) [Reeves et al., 2013], which is insufficient to reach the given K of 0.03 $G^{1/2}R_E$. A combination of these two factors accounts for the large PSD gaps in Panel (a1).

3. Event Simulation

3.1. Radial Diffusion Model

To simulate the magnetopause shadowing loss and the associated outward radial diffusion of electrons during the June 2015 dropout event, we apply a radial diffusion model that solves the equation:

$$\frac{\partial f}{\partial t} = L^2 \frac{\partial}{\partial L}\left(\frac{D_{LL}}{L^2}\frac{\partial f}{\partial L}\right) - \frac{f}{\tau}$$

where f is electron PSD at fixed μ and K values, L is the Roederer L or L*, D_{LL} is radial diffusion coefficient, and τ is electron e-folding lifetime. To represent the loss effects of magnetopause shadowing, electron lifetimes outside the LCDS are set to be on the order of electron drift periods (which are energy and pitch angle dependent [Schulz and Lanzerotti, 1974]), and event-specific LCDS calculated using the TS04 model driven by real time solar wind conditions is implemented (as shown in Figure 1(b3)). The model outer boundary is defined at

L*=11 (with Neumann boundary condition $\partial f/\partial L = 0$) which is always outside the LCDS during the event. The model initial condition as a function of L* is derived from the first available PSD data during the event. For D_{LL} we start with the commonly used empirical D_{LL} as a function of Kp index and L (approximately regarded as L*) with the magnetic component from Brautigam and Albert [2000] and the electric component from Brautigam et al. [2005], named D_{LL}(B&A) for short.

3.2. Simulation Results in PSD

With the above setups, Panel (a2) of Figure 2 shows the simulation results at the same μ and K values of the PSD data in Panel (a1), with the white curve denoting the LCDS position. We find that the model well captures the fast magnetopause shadowing loss of electrons outside the LCDS. To perform a more detailed comparison with data, four different time intervals during the event are selected to calculate the averaged PSD vs. L* profiles within each interval. The time coverage of each interval is marked by the horizontal color bars at the top of Panels (a1) and (a2) and denoted in UT hours in Panel (b1). The evolution of PSD vs. L* profiles during these intervals is compared between the data and the model in Panels (b1) and (b2) respectively. The black curves are profiles during interval #1 which covers the period before the shocks and a short period after the first shock. The data and model show similar profiles with mostly positive PSD vs. L* gradient (slightly negative at L*>4.6 possibly due to the first shock). Then for interval #2, which encloses a small LCDS drop after the first shock (see the white curve in Panel (a2)), we find the model well captures the shadowing loss outside L*=4.4 (blue curves in Panels (b1) and (b2)). There is another dip of LCDS during interval #3, leading to further loss of electrons at L*>4 in the model (green curve in Panel (b2)), which is mostly consistent with the data (Panel (b1)). Finally, we approach interval #4, a two-hour interval right after the second strong shock with LCDS pushed to as low as L*=3.4 right after the shock and then recovering to L*=4 at the end of the interval (see the white curve in Panel (a2)). Due to the very low LCDS values as well as the limited pitch angle coverage of the measured fluxes, there are very limited PSD data during this interval (the red curve in Panel (b1) stops at L*=3.1). On the other hand, the model (Panel (b2)) shows a fast shadowing loss at large L* and an internal PSD peak at low L*. This is consistent with the classic shadowing loss picture suggested by, e.g., Shprits et al. [2006] and Turner et al. [2012], where the shadowing first wipes out electrons outside the low LCDS, then as LCDS relaxes to larger L* the electrons diffuse both inward and outward creating an internal PSD peak. However, by comparing the red curves in Panels (b1) and (b2), we find the model results show an increase of PSD at L*<3.5 from the previous interval while the data shows no change, which suggests that the inward radial diffusion of electrons in the model could be too fast.

To more accurately specify radial diffusion in the model, one option is to replace D_{LL}(B&A),

which is based on a small set of datasets from the ground and space (ATS 6 and CRRES satellites), with a new D_{LL} model that is derived from larger and more recent datasets. Specifically, we choose the new electric diffusion coefficient, D_{LL}^E, from Liu et al. [2016] based on seven years of THEMIS data and the new magnetic diffusion coefficient, D_{LL}^B, from Ali et al. [2016] based on three years of Van Allen Probes data. Then the total $D_{LL} = D_{LL}^E + D_{LL}^B$ is named D_{LL}(Liu+Ali) for short. Panels (a4) and (a5) of Figure 2 show a comparison between D_{LL}(B&A) and D_{LL}(Liu+Ali) plotted vs. time and L, and Panel (a6) plots the ratio between them. We find that D_{LL}(Liu+Ali) is generally smaller than D_{LL}(B&A), especially during and after the second strong shock. The new simulation results after applying the new D_{LL}(Liu+Ali) are shown in Panels (a3) and (b3). Since the new D_{LL} is smaller, the model performance at low L* regions during interval #4 is greatly improved, suggesting that the new and more realistic D_{LL} is critical to capture the shadowing loss features during the event.

Due to limited PSD data coverage after the second strong shock, we can only validate the model results at L*<3.1 during interval #4 and the inbound passes of both probes are averaged to reach the PSD profile during that interval. Therefore, the two-step losses of the storage ring at low L* regions cannot be sufficiently studied using the PSD profiles. To recover the data coverage and better understand the loss mechanisms at both high and low L* regions, we compare the electron fluxes at given electron energy and pitch angle in the next section.

3.3. Simulation Results in Flux

Figure 3 (a1) and (a2) compare the observed and modeled electron fluxes at 5.2 MeV and 90^{o} local pitch angle. Panel (a1) shows the observed fluxes vs. time and L* with less data gaps only due to open electron drift shells (no L*). Panel (a2) plots the modeled fluxes extracted at Van Allen Probes' orbits, which are converted from the modeled PSD with D_{LL}(Liu+Ali) using the TS04 model. Again, we find our model captures the magnetopause shadowing loss well at large L*. The flux data have enough coverage to be compared with the model, per inbound or outbound pass of the spacecraft. We select eight passes of the two probes as marked by numbers in Panels (a1) and (a2) and shown in different colors in Panels (b1) and (b2), which compare the evolution of the radial flux profiles (in L*) from the data and model. The first two passes (#1 and #2) by Probes A and B respectively in Panel (b1) observed a double-peaked flux structure with the outer peak at L*~4.5 and the inner peak for the storage ring at L*~2.8, which is well captured by the model in Panel (b2). Then passes #3 and #4 show the shadowing losses at large L* regions after the first shock, which are also reproduced by the model. The flux vs. L* profiles do not show a significant change in the subsequent passes #5 and #6, consistent between the data and the model. Note the plateaus of the flux data at L*>4.7 in Panel (b1) are at the background level of REPT instrument.

Before moving on to the next pass after the second shock, we recall that the LCDS shows a strong K-dependence between the two shocks (Figure 1 (b3)), which leads to butterfly pitch angle distributions of fluxes observed at the apogees of Van Allen Probes (Figure 1 (b4)). In Panels (c1) and (c2) of Figure 3 we compare the observed and modeled pitch angle distributions of electron fluxes at 1.8 MeV along Probe A's orbit. The butterfly pitch angle distributions observed at the apogees between the two shocks are shown to be well captured by the model, even though the losses are slightly overestimated in the modeled fluxes.

Back to the evolution of flux vs. L* profiles, pass #7, observed by the leading Probe A right after the arrival of the second strong shock, shows a fast depletion of fluxes at L*>3.5, which is reproduced by the model with magnetopause shadowing. Looking at the inner flux peak at L*~2.8 (the storage ring), the observed fluxes in Panel (b1) also show a moderate decrease from pass #6 to #7, which is the initial drop of the two-step loss processes of the storage ring described in Section 1. These two-step losses were not discussed in the PSD comparison in Section 3.2 due to limited data coverage. However, by looking closer in Panel (a1) of Figure 2, we find that right after the second shock the PSD data observed by Probe A do not show a decrease at low L*. Consequently, the PSD profiles in Panel (b1) of Figure 2 show almost no change from interval #3 to #4. The unchanged PSD at given μ and K suggests that the flux drop from pass #6 to #7 is mostly adiabatic. By checking the local magnetic field observed during pass #7 at low L* regions, we find the magnetic field strength indeed decreases by a factor of two compared to previous pass, which can lead to an adiabatic decrease of flux at given electron energy (corresponding to higher μ thus lower PSD or flux). Comparing with the model results in Panels (a2) and (b2), we find this initial adiabatic flux drop of the storage ring from pass #6 to #7 is well captured by the model based on the PSD to flux conversion using the TS04 model.

Moving on to pass #8 observed by Probe B at about an hour later, in Panel (b1) we see a further flux drop of the storage ring at low L* regions, completing the two-step loss process. However, the model results in Panel (b2) show almost no change. To further investigate the energy dependence of the observed loss from pass #7 to #8, we plot the evolution of the observed electron energy spectrum in Panel (d). Observations show that the losses occur at E>1.8 MeV, with larger losses at higher energies. This is consistent with the energy dependence of EMIC wave scattering [e.g., Meredith et al., 2003; Summers et al., 2007; Ni et al., 2015]. Indeed, strong H^+ band EMIC waves were observed by Van Allen Probe A during pass #7 at L*=2.2-3.2 (see Figure 5 of Xiang et al. [2017]). Therefore, this subsequent electron loss observed by Probe B in pass #8 could be due to interactions with EMIC waves. It is not captured by our radial diffusion model since the model only focuses on magnetopause shadowing loss and does not include the scattering effects by EMIC waves.

4. Conclusions and Discussions

Remarkable dropout of relativistic and ultrarelativistic electrons at both high and low L regions were observed by the Van Allen Probes during the intense CME-driven June 2015 storm. Here for the first time an improved radial diffusion model with event-specific and K-dependent LCDS and newly available D_{LL} is implemented to quantitatively simulate the magnetopause shadowing loss of electrons during the dropout event. The major findings are concluded as follows:

1. The fast dropout of 1.8-6.3 MeV electrons observed at high L* regions after both interplanetary shocks are dominated by magnetopause shadowing loss due to low LCDS values. These observed losses are well reproduced by our radial diffusion model which shows that the model inputs of event-specific and K-dependent LCDS and new and realistic D_{LL} are critical to reproduce the detailed dropout features, including the observed timing and location of the dropout and the butterfly pitch angle distribution of electrons.

2. A two-step loss process of the high-energy storage ring (4.2-7.7 MeV) at low L* regions was observed after the second strong shock. Our model results well capture the initial loss observed by the leading probe right after the shock and demonstrate that the initial drop is adiabatic in nature.

3. Further depletion of the high-energy storage ring observed by the trailing probe at about an hour later is suggested to be caused by EMIC wave scattering based on the observed energy

dependence. It is not captured by the current model which only focuses on magnetopause shadowing losses.

To further improve our model in the future, especially to capture the non-adiabatic depletion of the high-energy storage ring, the mechanism of pitch angle scattering by EMIC waves needs to be included. Due to the limited coverage of equatorial pitch angles in the observed electron fluxes, we cannot sufficiently validate if the pitch angle dependence of the observed loss is consistent with EMIC wave scattering. In addition, Xiang et al. [2017] and Qin et al. [2019] both calculated the minimum resonant energy of the observed H^+ band EMIC waves and found it to be in the range of 4 to 5 MeV. Therefore, the observed loss of the storage ring at lower energies shown in Figure 3(c) could be due to scattering by other types of magnetospheric waves which also needs to be investigated in the future. Furthermore, the newly available D_{LL}(Liu+Ali) used in our model, even though demonstrated to be sufficient to explain the observed fast shadowing loss of electrons during the event, is still empirical. Recently, event-specific D_{LL} based on real-time measurements of ultra-low frequency waves have been developed [e.g., Mann et al., 2016; Ozeke et al., 2017; Olifer et al., 2019]. In the future, event-specific D_{LL} coordinated in L* need to be implemented in the model in tandem with the K-dependent LCDS.

Acknowledgments

This work was supported by NSF grant AGS 1752736 and NASA grants NNX15AW06G, 80NSSC18K1284, and 80NSSC19K0908. Contributions by S. K. Morley were performed under the auspices of DOE and were partially supported by the Laboratory Directed Research and Development (LDRD) program award 20150127ER. The authors would like to thank the NASA Van Allen Probes team for providing the REPT data and the Qin-Denton parameters for L* calculation (https://www.rbsp-ect.lanl.gov/science/DataDirectories.php). The model inputs and outputs in the paper are publicly available from the data repository of the Department of Physics and Astronomy at West Virginia University (https://ulysses.phys.wvu.edu/plasma/?q=node/214).

References

Albert, J. M., Selesnick, R. S., Morley, S. K., Henderson, M. G., & Kellerman, A. C. (2018). Calculation of last closed drift shells for the 2013 GEM radiation belt challenge events. *Journal of Geophysical Research: Space Physics,* 123, 9597–9611. https://doi.org/10.1029/2018JA025991

Ali, A. F., D. M. Malaspina, S. R. Elkington, A. N. Jaynes, A. A. Chan, J. Wygant, and C. A. Kletzing (2016), Electric and magnetic radial diffusion coefficients using the Van Allen probes data, *J. Geophys. Res. Space Physics, 121,* doi:10.1002/2016JA023002.

Baker, D. (2000), The occurrence of operational anomalies in spacecraft and their relationship to space weather, *IEEE Trans. Plasma Sci., 28*(6), 2007–2016, doi:10.1109/27.902228.

Baker, D. N., Kanekal, S. G., Hoxie, V. C., Batiste, S., Bolton, M., Li, X., ... & Westfall, J. (2013). The Relativistic Electron-Proton Telescope (REPT) instrument on board the Radiation Belt Storm Probes (RBSP) spacecraft: Characterization of Earth's radiation belt high-energy particle populations. Space Science Reviews, 179(1-4), 337-381. https://doi.org/10.1007/s11214-012-9950-9

Baker, D. N., Jaynes, A. N., Kanekal, S. G., Foster, J. C., Erickson, P. J., Fennell, J. F., et al. (2016), Highly relativistic radiation belt electron acceleration, transport, and loss: Large solar storm events of March and June 2015, *J. Geophys. Res. Space Physics*, 121, doi:10.1002/2016JA022502.

Brautigam, D. H., and J. M. Albert (2000), Radial diffusion analysis of outer radiation belt electrons during the 9 October 1990 magnetic storm, *J. Geophys. Res., 105*, 291–309, doi:10.1029/1999JA900344.

Brautigam, D. H., G. P. Ginet, J. M. Albert, J. R. Wygant, D. E. Rowland, A. Ling, and J. Bass (2005), CRRES electric field power spectra and radial diffusion coefficients, *J. Geophys. Res., 110,* A02214, doi:10.1029/2004JA010612.

Finlay, C., Maus, S., Beggan, C., Hamoudi, M., Lowes, F., Olsen, N., & Thébault, E. (2010). Evaluation of candidate geomagnetic field models for IGRF-11. *Earth, Planets and Space, 62(10),* 787–804. https://doi.org/10.5047/eps.2010.11.005

Lanzerotti, L. J. (2001), Space weather effects on communications, in *Space Storms and Space Weather Hazards*, edited by I. A. Daglis, *NATO Sci. Ser., Ser. II, 38*, 313–334.

Liu, W., W. Tu, X. Li, T. Sarris, Y. Khotyaintsev, H. Fu, H. Zhang, and Q. Shi (2016), On the calculation of electric diffusion coefficient of radiation belt electrons with in situ electric field measurements by THEMIS, *Geophys. Res. Lett., 43,* 1023–1030, doi:10.1002/2015GL067398.

Loto'aniu, T. M., Singer, H. J., Waters, C. L., Angelopoulos, V., Mann, I. R., Elkington, S. R., & Bonnell, J. W. (2010). Relativistic electron loss due to ultralow frequency waves and enhanced outward radial diffusion. Journal of Geophysical Research, **115**, A12245. https://doi.org/10.1029/2010JA015755

Mann, I. R., et al. (2016), Explaining the dynamics of the ultra-relativistic third Van Allen radiation belt, Nat. Phys., doi:10.1038/nphys3799.

McIlwain, C. E. (1961). Coordinates for mapping the distribution of magnetically trapped particles. *Journal of Geophysical Research*, *66*, 3681–3691. https://doi.org/10.1029/JZ066i011p03681

Meredith, N. P., Thorne, R. M., Horne, R. B., Summers, D., Fraser, B. J., & Anderson, R. R. (2003). Statistical analysis of relativistic electron energies for cyclotron resonance with EMIC waves observed on CRRES. Journal of Geophysical Research: Space Physics, 108(A6), 1250 https://doi.org/10.1029/2002JA009700

Millan, R. M. and D. N. Baker (2012), A nergies in Earth's radiation belts, *Space Sci. Rev.*, 173, 103–131, doi:10.1007/s11214 - 012 - 9941 - x.

Morley, S. K., Friedel, R. H. W., Cayton, T. E., & Noveroske, E. (2010a). A rapid, global and prolonged electron radiation belt dropout observed with the Global Positioning System constellation. *Geophysical Research Letters*, *37*(6).

Morley, S. K. et al. (2010b), Dropouts of the outer electron radiation belt in response to solar wind stream interfaces: Global positioning system observations. Proc. R. Soc. A 466, 3329-3350.

Ni, B., Cao, X., Zou, Z., Zhou, C., Gu, X., Bortnik, J., ... & Xie, L. (2015). Resonant scattering of outer zone relativistic electrons by multiband EMIC waves and resultant electron loss time scales. Journal of Geophysical Research: Space Physics, 120, 7357-7373. https://doi.org/10.1002/2015JA021466

Olifer, L., Mann, I. R., Morley, S. K., Ozeke, L. G., & Choi, D. (2018). On the role of last closed drift shell dynamics in driving fast losses and Van Allen radiation belt extinction. *Journal of Geophysical Research: Space Physics, 123.* https://doi.org/10.1029/2018JA025190

Olifer, L., Mann, I. R., Ozeke, L. G., Rae, I. J., & Morley, S. K. (2019). On the relative strength of electric and magnetic ULF wave radial diffusion during the March 2015 geomagnetic storm. *Journal of Geophysical Research: Space Physics,* 124. https://doi.org/10.1029/2018JA026348

Olson, W. P., & Pfitzer, K. A. (1977). *Magnetospheric magnetic field modeling Ann. Sci. Rep. F44620-75-C-0033.* Arlington, Va: Air Force Off. Of Sci. Res.

Onsager, T. G., G. Rostoker, H.-J. Kim, G. D. Reeves, T. Obara, H. J. Singer, and C. Smithtro (2002), Radiation belt electron flux dropouts: Local time, radial, and particle-energy dependence, *J. Geophys. Res.*, *107*(A11), 1382, doi:10.1029/2001JA000187.

Ozeke, L. G., Mann, I. R., Murphy, K. R., Sibeck, D. G., & Baker, D. N. (2017). Ultra -

relativistic radiation belt extinction and ULF wave radial diffusion: Modeling the September 2014 extended dropout event. *Geophysical Research Letters, 44*(6), 2624-2633. https://doi.org/10.1002/2017GL072811

Qin, M., Hudson, M., Li, Z., Millan, R., Shen, X., Shprits, Y., et al (2019). Investigating loss of relativistic electrons associated with EMIC waves at low L values on 22 June 2015. *Journal of Geophysical Research: Space Physics*, 124. https://doi.org/10.1029/2018JA025726

Reeves, G. D., et al. (2013), Electron acceleration in the heart of the Van Allen radiation belts, *Science,* 341(6149), 991–994, doi:10.1126/science.1237743.

Roederer, J. G. (1970). Dynamics of geomagnetically trapped radiation. New York: Springer.

Schulz, M., and L. Lanzerotti (1974), *Particle Diffusion in the Radiation Belts,* Springer, New York.

Shprits, Y. Y., R. M. Thorne, R. Friedel, G. D. Reeves, J. Fennell, D. N. Baker, and S. G. Kanekal (2006), Outward radial diffusion driven by losses at magnetopause, *J. Geophys. Res.,* 111, A11214, doi:10.1029/2006JA011657.

Shprits, Y. Y., et al. (2008a), Review of modeling of loses and sources of relativistic electrons in the outer radiation belt. I: Radial transport, *J. Atmos. Sol. Terr. Phys.,* 70, 1679, doi:10.1016/j.jastp.2008.06.008.

Shprits, Y. Y., et al. (2008b), Review of modeling of loses and sources of relativistic electrons in the outer radiation belt. II: Local acceleration and loss, *J. Atmos. Sol. Terr. Phys.*, 70, 1694–1713, doi:10.1016/j.jastp.2008.06.014.

Shprits, Y. Y., Drozdov, A. Y., Spasojevic, M., Kellerman, A. C., Usanova, M. E., Engebretson, M. J., ... & Baker, D. N. (2016). Wave-induced loss of ultra-relativistic electrons in the Van Allen radiation belts. Nature communications, 7, 12883. https://doi:10.1038/ncomms12883

Summers, D., Ni, B., & Meredith, N. P. (2007). Timescales for radiation belt electron acceleration and loss due to resonant wave -particle inter

chorus, ELF hiss, and electromagnetic ion cyclotron waves. Journal of Geophysical Research: Space Physics, 112, A04207. https://doi.org/10.1029/2006JA011993

Tsyganenko, N. A., & Sitnov, M. I. (2005). Modeling the dynamics of the inner magnetosphere during strong geomagnetic storms. Journal of Geophysical Research: Space Physics, 110, A03208. https://doi.org/10.1029/2004JA010798

Tu, W., Li, X., Chen, Y., Reeves, G. D., & Temerin, M. (2009). Storm -dependent ra

electron dynamics. Journal of Geophysical Research: Space Physics, 114(A2). A02217. https://doi.org/10.1029/2008JA013480

Tu, W., Selesnick, R., Li, X., & Looper, M. (2010). Quantification of the precipitation loss of radiation belt electrons observed by SAMPEX. Journal of Geophysical Research: Space Physics, 115(A7), A07210. https://doi.org/10.1029/2009JA014949

Tu, W., Cunningham, G. S., Chen, Y., Morley, S. K., Reeves, G. D., Blake, J. B., ... & Spence, H. (2014). Event -specific chor

using the Van Allen Probes. Geophysical Research Letters, 41, 1359-1366. https://doi.org/10.1002/2013GL058819

Turner, D. L., Shprits, Y., Hartinger, M., & Angelopoulos, V. (2012). Explaining sudden losses of outer radiation belt electrons during geomagnetic storms. Nature Physics, 8, 202-212. https://doi:10.1038/nphys2185

Xiang, Z., Tu, W., Li, X., Ni, B., Morley, S. K., & Baker, D. N. (2017). Understanding the mechanisms of radiation belt dropouts observed by Van Allen Probes. Journal of Geophysical Research: Space Physics, 122, 9858–9879. https://doi.org/10.1002/2017JA024487

Xiang, Z., Tu, W., Ni, B., Henderson, M. G., & Cao, X. (2018). A statistical survey of radiation belt dropouts observed by Van Allen Probes. *Geophysical Research Letters, 45.* https://doi.org/10.1029/2018GL078907

Figures and Captions

Figure 1. (a1)-(a3): Electron fluxes (in units of $(\mathrm{cm}^2\ \mathrm{s\ sr\ keV})^{-1}$) at 90^o local pitch angle vs. L and time observed by REPT during June 22-23, 2015, at energies of 1.8, 4.2, and 6.3 MeV respectively; (a4), (b1), and (b2): Dst index, IMF B_z, and solar wind dynamic pressure respectively; (b3): Electron LCDS at different K values in different colors calculated using TS04 model; (b4): 1.8 MeV electron fluxes vs. time and local pitch angle observed by Van Allen Probe A along its orbit. The two vertical red lines mark the arrivals of two interplanetary shocks.

Figure 2. (a1)-(a3): Electron PSD data (in units of $(\mathrm{c/MeV/cm})^3$) and simulation results at μ=1318 MeV/G and K=0.03 $G^{1/2}R_E$, with the black curve in (a1) and white curves in (a2)-(a3) showing the LCDS locations and the two vertical red curves marking the two shocks; (a4)-(a6): D_{LL}(B&A), D_{LL}(Liu+Ali), and ratio D_{LL}(B&A)/D_{LL}(Liu+Ali) plotted vs. time and L; (b1)-(b3): Observed and simulated PSD vs. L* profiles from Panels (a1)-(a3) averaged over four different time intervals. Specifically, (a2) and (b2) are from model results with D_{LL}(B&A), and (a3) and (b3) are with D_{LL}(Liu+Ali).

Figure 3. (a1)-(a2): Observed and modeled electron fluxes at 5.2 MeV and 90^o local pitch angle at Van Allen Probes' orbits during June 22-23, 2015 with the two vertical red lines marking the two shocks; (b1)-(b2): Observed and simulated flux vs. L* profiles during eight passes of the two probes as marked in (a1)-(a2); (c1)-(c2): Observed and modeled pitch angle distributions of

electron fluxes at 1.8 MeV along Probe A’s orbit with the two vertical black lines marking the two shocks; (d): Evolution of the observed electron energy spectrum from pass #7 to #8.

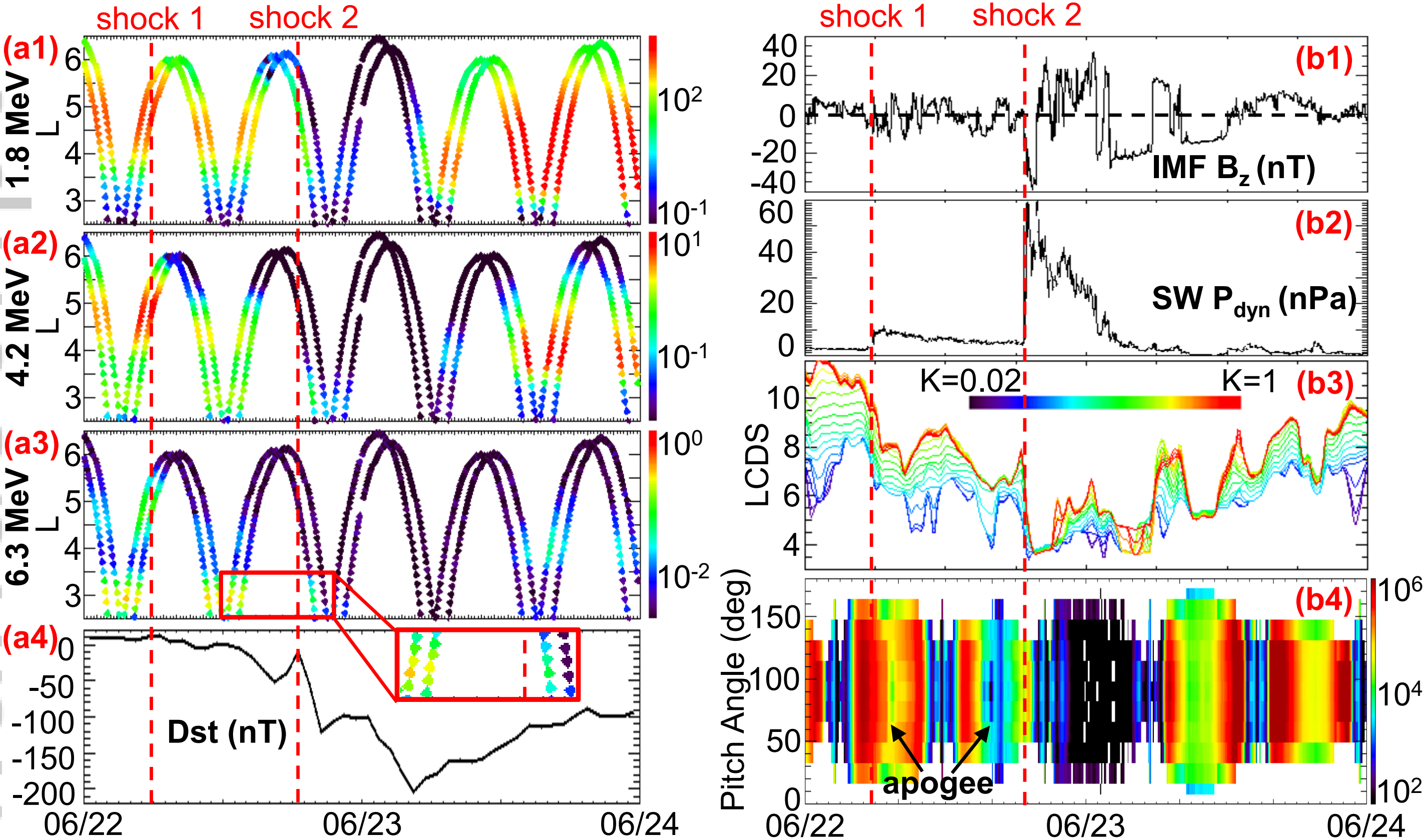
shock 1
shock 2
(a1)
1.8 MeV
L
6
5
4
3
10^2
10^-1
(a2)
4.2 MeV
L
6
5
4
3
10^1
10^-1
(a3)
6.3 MeV
L
6
5
4
3
10^0
10^-2
(a4)
0
-50
-100
-150
-200
Dst (nT)
06/22
06/23
06/24
shock 1
shock 2
(b1)
40
20
0
-20
-40
IMF B_z (nT)
(b2)
60
40
20
0
SW P_dyn (nPa)
(b3)
K=0.02
K=1
LCDS
10
8
6
4
(b4)
Pitch Angle (deg)
150
100
50
0
10^6
10^4
10^2
apogee
06/22
06/23
06/24

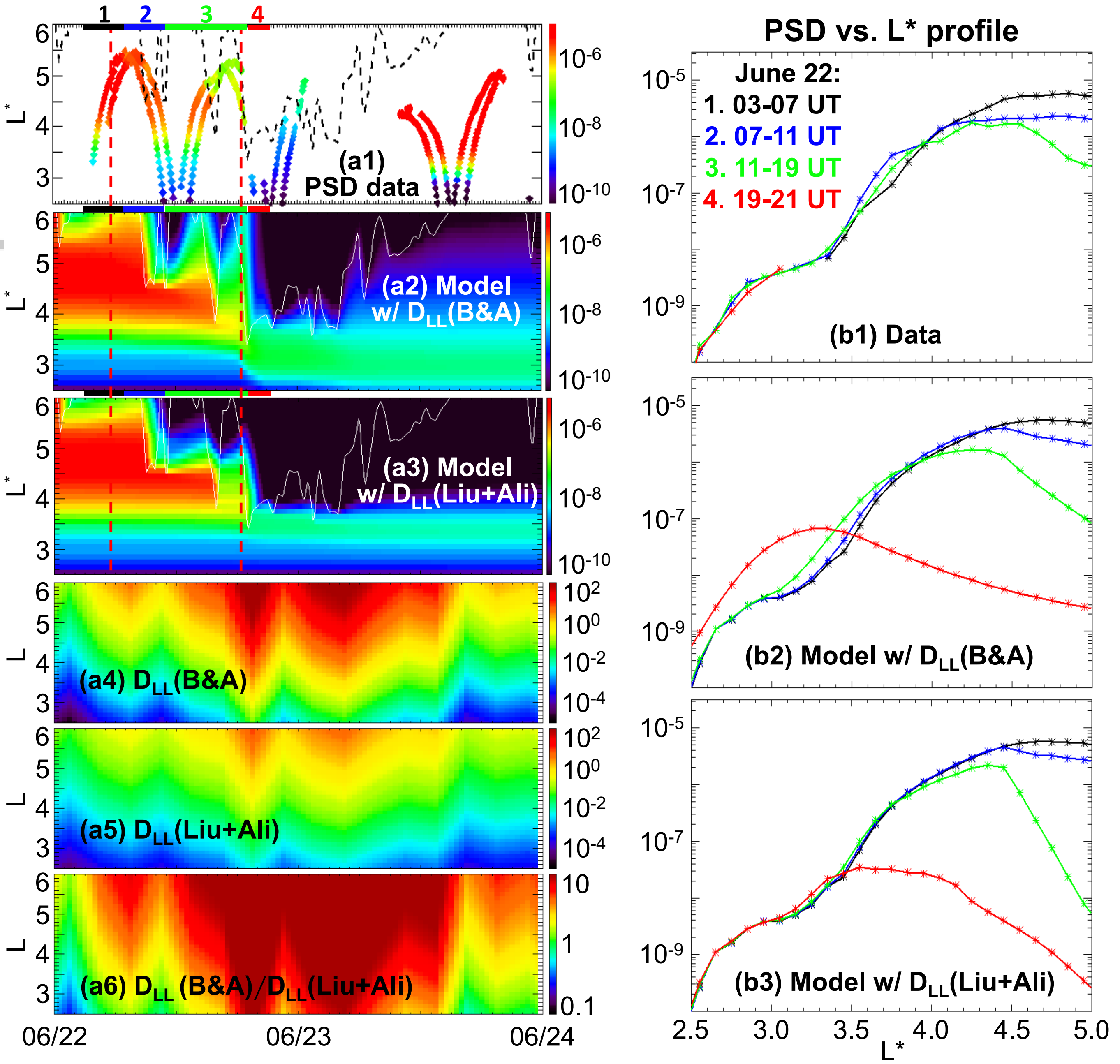
1
2
3
4
(a1) PSD data
(a2) Model w/ D_{LL}(B&A)
(a3) Model w/ D_{LL}(Liu+Ali)
(a4) D_{LL}(B&A)
(a5) D_{LL}(Liu+Ali)
(a6) D_{LL} (B&A)/D_{LL}(Liu+Ali)
L^*
L
6
5
4
3
10^{-6}
10^{-8}
10^{-10}
10^2
10^0
10^{-2}
10^{-4}
10
1
0.1
06/22
06/23
06/24
PSD vs. L* profile
June 22:
1. 03-07 UT
2. 07-11 UT
3. 11-19 UT
4. 19-21 UT
(b1) Data
(b2) Model w/ D_{LL}(B&A)
(b3) Model w/ D_{LL}(Liu+Ali)
10^{-5}
10^{-7}
10^{-9}
2.5
3.0
3.5
4.0
4.5
5.0
L^*

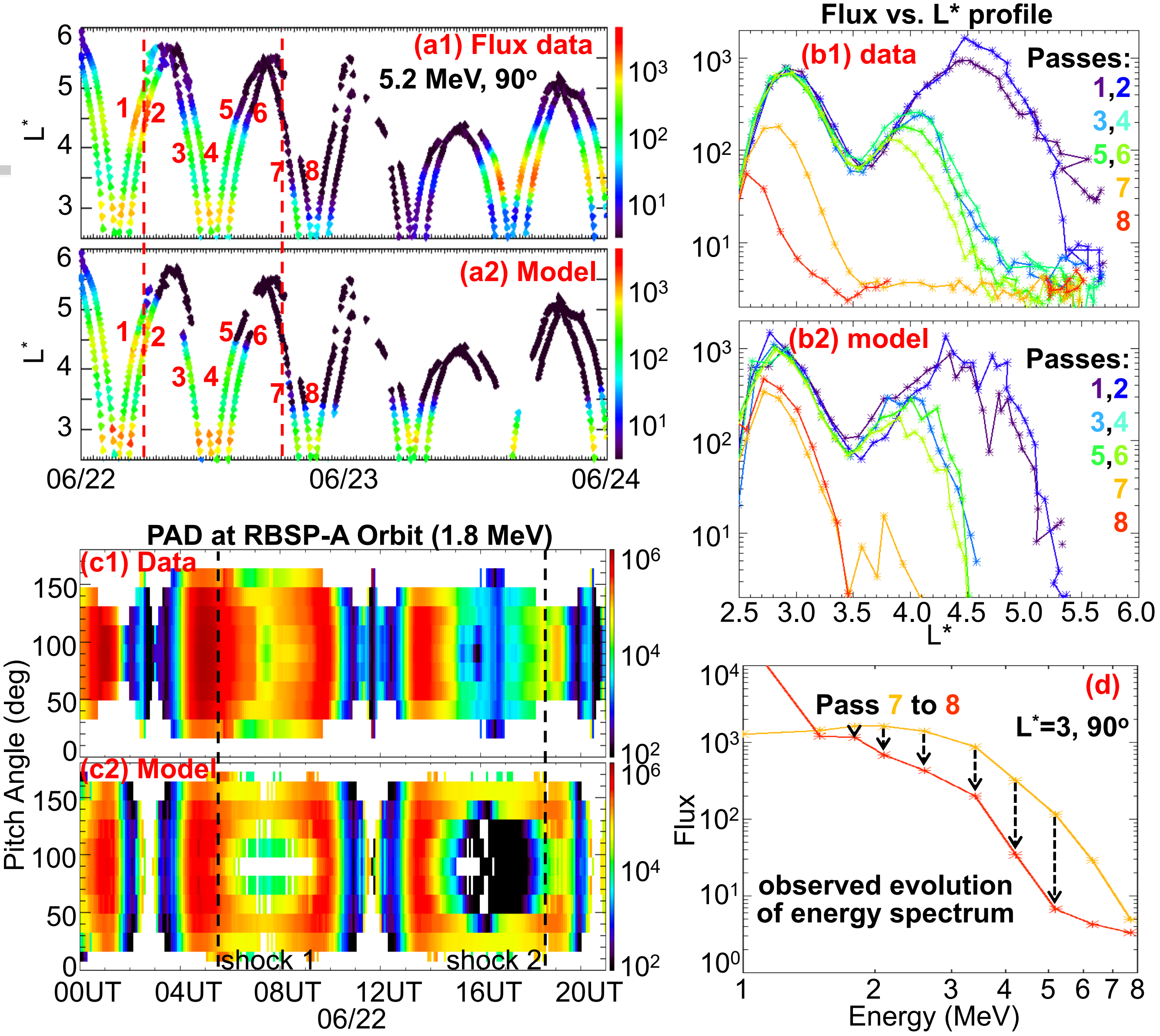
(a1) Flux data
5.2 MeV, 90°
(a2) Model
L*
1 2 3 4 5 6 7 8
10¹ 10² 10³
06/22 06/23 06/24
Flux vs. L* profile
(b1) data
(b2) model
Passes:
1,2
3,4
5,6
7
8
10¹ 10² 10³
2.5 3.0 3.5 4.0 4.5 5.0 5.5 6.0
L*
PAD at RBSP-A Orbit (1.8 MeV)
(c1) Data
(c2) Model
Pitch Angle (deg)
0 50 100 150
10² 10⁴ 10⁶
shock 1
shock 2
00UT 04UT 08UT 12UT 16UT 20UT
06/22
(d)
Pass 7 to 8
L*=3, 90°
observed evolution of energy spectrum
Flux
10⁰ 10¹ 10² 10³ 10⁴
1 2 3 4 5 6 7 8
Energy (MeV)